CANCER

In vitro engineering of a bone metastases model allows for study of the effects of antiandrogen therapies in advanced prostate cancer

Nathalie Bock[1,2,3,4,5], Thomas Kryza[1,2,3†‡], Ali Shokoohmand[1,2,3,4†], Joan Röhl[1,2,3], Akhilandeshwari Ravichandran[2,3,4], Marie-Luise Wille[2,5,6], Colleen C. Nelson[1,2,3], Dietmar W. Hutmacher[1,3,4,5,6,7*], Judith A. Clements[1,2,3*]

While androgen-targeted therapies are routinely used in advanced prostate cancer (PCa), their effect is poorly understood in treating bone metastatic lesions and ultimately results in the development of metastatic castrate resistant prostate cancer (mCRPC). Here, we used an all-human microtissue-engineered model of mineralized metastatic tissue combining human osteoprogenitor cells, 3D printing and prostate cancer cells, to assess the effects of the antiandrogens, bicalutamide, and enzalutamide in this microenvironment. We demonstrate that cancer/bone stroma interactions and antiandrogens drive cancer progression in a mineralized microenvironment. Probing the bone microenvironment with enzalutamide led to stronger cancer cell adaptive responses and osteomimicry than bicalutamide. Enzalutamide presented with better treatment response, in line with enzalutamide delaying time to bone-related events and enzalutamide extending survival in mCRPC. The all-human microtissue-engineered model of mineralized metastatic tissue presented here represents a substantial advance to dissect the role of the bone tumor microenvironment and responses to therapies for mCPRC.

INTRODUCTION

Bone metastatic lesions are found in over 90% of patients with metastatic castrate resistant prostate cancer (mCRPC), resulting in multifocal pain and pathological fractures, responsible for many deaths (*1*). Several drugs have been Food and Drug Administration–approved for mCPRC, yet with little survival benefits (*2*). While none of these androgen-targeted therapies (ATTs) are curative, they do provide survival advantages and are widely clinically used. Androgen signaling is key to all prostate cancer stages (*3*), and thus, targeting the androgen axis continues to be the gold standard for recurrent advanced disease (*4*), with enzalutamide treatment one of the most used currently (*5*), in sequence with cytotoxic chemotherapy and bone-targeting agents (*2*). Yet, although recent data suggest that targeting the tumor cells and the bone microenvironment improves survival (*6*), the role of the tumor microenvironment as a key modulator of tumor cell response to therapy is still unclear. While the use of androgen receptor (AR) antagonists initially inhibits or delays bone metastasis (*7*), ATT ultimately lead to both cancer cell and stroma adaptation through a combination of AR reactivation (*8*) and paracrine signaling. With mechanisms not fully understood, ATT may further promote metastasis progression and adverse outcomes. Since bone metastasis is mostly always present in the castration-resistant phase (*9*), it is critical to closely delineate the actual effects of standard ATT such as AR antagonists in the bone tumor microenvironment (*10*).

Bone metastases in prostate cancer are predominantly bone forming (*6*), referred to as osteoblastic/osteosclerotic, although osteoclasts have been proposed as the key to the initiation of the vicious cycle in mCRPC by releasing growth factors (GFs) such as transforming GF–β and insulin-like GFs (IGFs), which attract prostate cancer cells (*6*). In turn, cancer cells are responsible for the establishment of a microenvironment inducing stem cell osteogenic differentiation (*4*) and osteoblast activation (*11*) by the direct secretion of GFs (IGF, endothelin-1, and platelet-derived GF) as well as by controlling the localization and activity of multiple soluble factors through the production of proteases, including matrix metalloproteinases 7 and 9 (*12*). While some mechanisms have been proposed, the factors involved in the cross-talk between cancer cells and the bone microenvironment, especially in the context of ATT and acquired ATT resistance (*10*), still have not been identified. Understanding the molecular actors involved in the adaptation of the bone tumor microenvironment to ATT is crucial for the identification of rational molecular targets and the development of more effective therapeutic agents for mCRPC.

The main challenge is adequately modeling the pathology of the disease in vitro (*13*). Current models of bone metastases, even defined by their inventors as advanced, including microfluidic devices or rotary culture systems, lack reproducibility or physiological relevance (*14*), partly due to limited cell-to-cell and cell-to-matrix interactions. They also lack the required capability to study treatment effects in long-term cultures, combined with quantitative imaging and high throughout processing at a single-cell level (*15*). In our previous work, we have developed and validated a highly reproducible microtissue-engineered in vitro human construct that comprises osteoblasts and osteocytic cells, with relevant protein expression and mineral content. The mature mineralized engineered tissue could be cultured for up to 12 weeks in vitro (*16*). We successfully

[1]School of Biomedical Sciences, Faculty of Health and Australian Prostate Cancer Research Centre (APCRC-Q), Brisbane 4000, QLD, Australia. [2]Institute of Health and Biomedical Innovation (IHBI), Queensland University of Technology (QUT), Brisbane 4000, QLD, Australia. [3]Translational Research Institute (TRI), QUT, Woolloongabba, 4102 QLD, Australia. [4]Centre in Regenerative Medicine, IHBI, QUT, Kelvin Grove, 4059 QLD, Australia. [5]Australian Research Council (ARC) Training Centre for Multiscale 3D Imaging, Modelling and Manufacturing (M3D Innovation), QUT, Kelvin Grove, 4059 QLD, Australia. [6]Bone and Joint Disorders Program, School of Mechanical Medical, and Process Engineering, Science and Engineering Faculty (SEF), QUT, Brisbane, 4000 QLD, Australia. [7]ARC Training Centre in Additive Biomanufacturing, QUT, Kelvin Grove, 4059 QLD, Australia.
*Corresponding author. Email: dietmar.hutmacher@qut.edu.au (D.W.H.); j.clements@qut.edu.au (J.A.C.)
†These authors contributed equally to this work.
‡Present address: Mater Research Institute, The University of Queensland, Translational Research Institute, Woolloongabba, Queensland, Australia.

used the mineralized microtissue in coculture with metastatic prostate cancer cell lines (LNCaP, C4-2B, and PC3 cells) and showed that this model could reproduce some of the cellular alterations seen in vivo under androgen deprivation, followed by unprecedented three-dimensional (3D) morphometric and functional characterization at the cellular level (*16*). Furthermore, the mineralized microtissue was combined with prostate cancer patient–derived xenografts in an indirect mode, revealing in vitro osteomimicry from paracrine interactions between the tumor and the bone microenvironment. The microtissue thus presented with versatility and relevance in recapitulating the key processes seen in vivo using patient-derived tissues (*17*).

In the current study, we hypothesized that traditional antiandrogens have limited effects in the bone tumor microenvironment and may be a source of downstream adaptive responses that can fuel the survival and growth of bone metastases. Specifically, we used the previously developed human model to determine the quantitative outcomes of the first-generation (bicalutamide) and the second-generation (enzalutamide) antiandrogen drugs on prostate cancer osteoblastic metastases, combining 4D live microscopy, cell morphometry, and gene and protein analysis.

RESULTS

A 3D microtissue model of human prostate cancer osteoblastic metastases

We combined additive manufacturing and tissue engineering to establish a primary human osteoblast–derived bone-like microtissue (hOBMT) as defined and characterized previously (*16*). The microtissue presented with high mineral content, embedded osteoblasts and fully differentiated osteocytes, and relevant bone-like markers and extracellular matrix (ECM) proteins. It was shown in this previous work how the 3D hOBMT constructs provide enhanced physiological relevance, as compared to various 2D control groups. The latter were unable to lead to osteocytogenesis and the expression of related key proteins. This included the expression of sclerostin only in the 3D hOBMT constructs, a key bone protein playing an important role in the receptor activator of nuclear factor κB/osteoprotegerin (RANK/OPG) pathways, ultimately affecting prostate cancer bone metastasis. The mineralized microtissues were further used in coculture with fluorescently tagged AR-positive/negative metastatic prostate cancer cell lines (LNCaP, C4-2B, and PC3 cells) and let to grow on hOBMT from 3 hours to 3 weeks depending on the targeted characterization. This resulted in a versatile in vitro model of human prostate cancer osteoblastic metastases, showing the effects of androgen deprivation in that microenvironment (*16*). Here, we used this model and methodologies (Fig. 1A) to assess the effects of dihydrotestosterone (DHT) depletion in media and common antiandrogen therapies, also referred to as ATT, enzalutamide (Enz), and bicalutamide (Bic) in the bone microenvironment. The use of Enz and Bic are currently undefined in this microenvironment yet critical to further understand their effects in patients with mCRPC lesions in bone. LNCaP and C4-2B cells were first preconditioned in 2D with the treatments for 7 days before coculture with the mineralized microtissues. Next, upon the initial 24-hour seeding period, the cancer cells successfully attached to the mineralized 3D microtissues with no major differences from drug-free preconditioning compared to DHT preconditioning for either LNCaP or C4-2B (Fig. 1B). No further differences in C4-2B cell attachment were observed with Enz/Bic preconditioning, yet LNCaP attachment was reduced from 50 ± 11% in DHT to 38 ± 12% ($P < 0.05$) and 32 ± 4% ($P < 0.01$), with Enz and Bic preconditioning, respectively (Fig. 1B), showing the positive effects of both antiandrogens at reducing AR-dependent cancer cell attachment in the bone microenvironment, in line with the clinical literature, where antiandrogens initially retard bone metastasis (*7*). As expected, the drug-free control showed similar adhesion to the DHT group and increased adhesion compared to the Enz and Bic conditions, as AR is activated by other factors, including interleukin-6 and IGFs, which are produced by bone cells (*11*). This AR activation creates a favorable response from cancer cells, whereas it is blocked in the Enz/Bic conditions. After 3 weeks coculture, all conditions led to cancer cell colonization of the hOBMT, up to 70% confluence in some conditions. An example of the resulting metastatic constructs cocultured for 3 weeks under Bic and Enz is shown in Fig. 1 (C to E), displaying direct interactions between osteoblasts and cancer cells. The developed constructs thus provide a relevant and viable bone metastatic platform for further analysis.

Antiandrogen treatments increase cancer cell volume and reduce sphericity in the bone microenvironment

The morphometric features of cancer cells inform on plasticity and potentially malignancy and thus can be used to evaluate a changing cellular phenotype in response to therapies (*18*). In prostate cancer, prolonged targeting of the AR is a known trigger to adaptive response with the activation of programs such as epithelial-to-mesenchymal transition (EMT) and neuroendocrine transdifferentiation (NEtD). This is evidenced by the expression of a defined molecular marker profile as well as specific cell morphologies, typically including elongated and spindle-shaped phenotypes (*19*). These phenotypes can be quantified by changes in cellular volume and usually decrease of sphericity and thus represent useful quantitative tools. Complexity, however, arises when quantifying individual cells in 3D coculture microenvironments, in both static and temporal fashions. We circumvented this effect by analyzing the LNCaP/C4-2B cells tagged with mKO2 and adhered to hOBMT, after 3 and 24 hours after seeding periods, to retain individual cells, which is necessary for single-cell analysis. We then used a research method that we developed to rapidly quantify in 3D a high number of individual cancer cells on top of hOBMT based on fluorescence (*20*). Briefly, by combining spinning disc confocal (SDC) microscopy for high-throughput 3D image collection (Fig. 2A) and the Imaris software for automated tracking and 3D segmentation (Fig. 2B), up to 1000 individual cells per condition are analyzed in a rapid manner. This provides strong statistical power, the latter a current problem in cell morphometry data analysis. We previously saw that androgen deprivation led to the highest adaptive response for the highest degree of AR responsiveness (LNCaP > C4-2B) after 24 hours (*16*). Here, we hypothesized that an adaptive response from 3 to 24 hours would be observed in both cell types. This was the case with significant overall increase in volume ($P < 0.0001$; Fig. 2C) and decrease in sphericity ($P < 0.001$; Fig. 2D) for both cell types and throughout treatments. Comparing LNCaP and C4-2B cell types on hOBMT, it was also seen that LNCaP cells had similar volumes within the first 24 hours but decreased sphericities, compared to C4-2B, as previously observed (*16*). This rightly suggests a more adaptive responsive from AR-dependent cells. We then hypothesized that the antiandrogen treatments would not be able to provide similar responses as the drug-free control group, due to compensating effects from the bone microenvironment. The

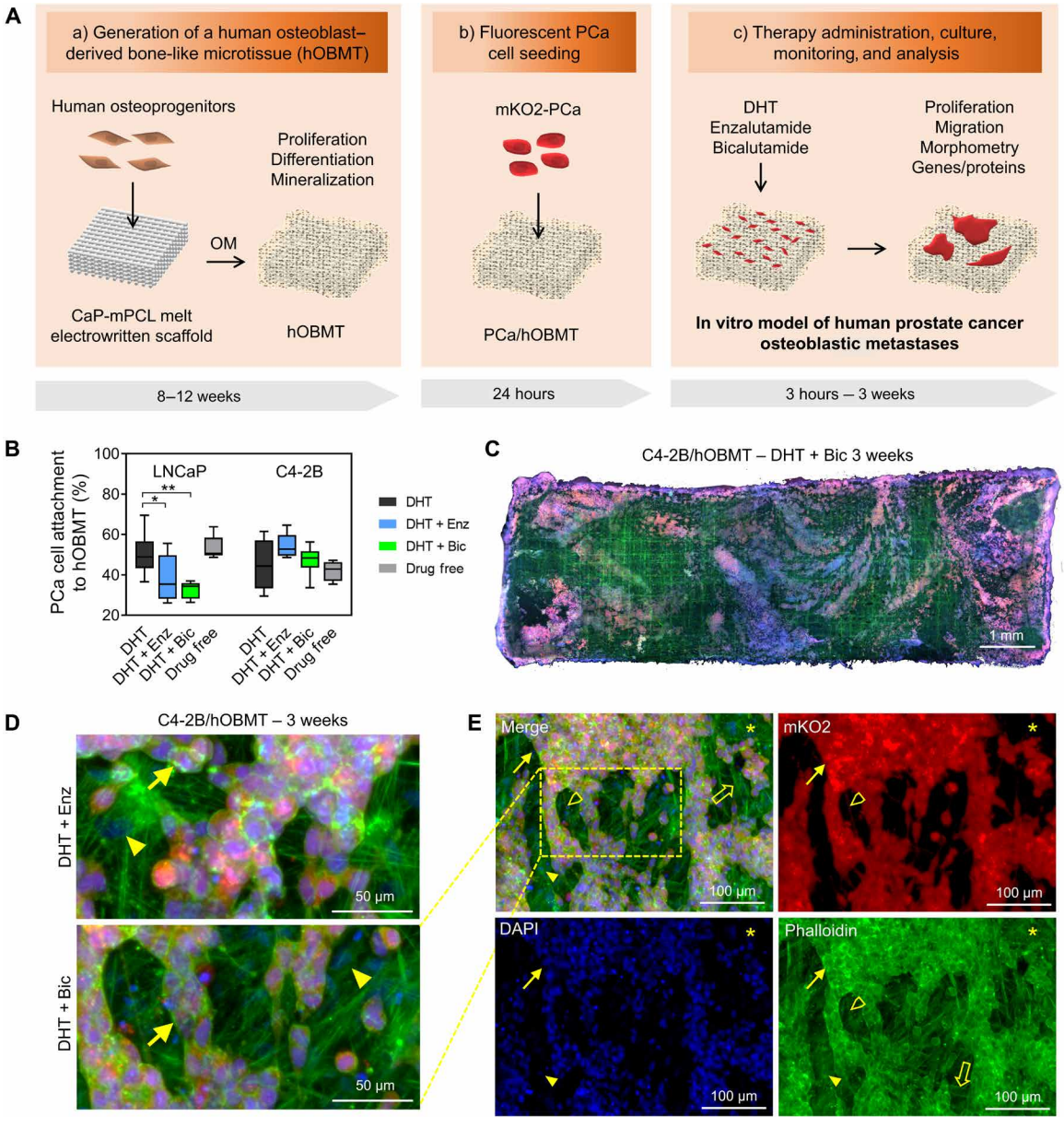

Fig. 1. Development of an in vitro microtissue-engineered 3D model of human prostate cancer osteoblastic metastases. (**A**) Schematic overview of manufacturing involving (a) a calcium phosphate–coated melt electrowritten polycaprolactone (CaP-mPCL) scaffold seeded with primary human osteoprogenitors, followed by 8 to 12 weeks culture in osteogenic media (OM), leading to an hOBMT; (b) coculture with fluorescently tagged (mKO2) prostate cancer (PCa) cell lines for 24 hours; and (c) therapy administration, culture from 24 hours to 3 weeks, monitoring and analysis. (**B**) Attachment rates (%) of LNCaP and C4-2B cells to hOBMT conditioned in DHT (dihydrotestosterone), DHT + Enz (enzalutamide), DHT + Bic (bicalutamide), or drug-free for 7 days before coculture with hOBMT for 24 hours (average $n = 5$), $^{*}P < 0.05$ and $^{**}P < 0.01$. (**C** to **E**) Confocal microscopy images of the 3D metastatic microtissues after 3 weeks hOBMT coculture with C4-2B cells under DHT (10 nM) and bicalutamide (Bic, 10 μM) (C to E) or DHT + enzalutamide (Enz, 10 μM) (D) showing cancer cell coverage of hOBMT and formation of micrometastases (MaxProj. shown, 50-μm z-stacks). Split channels show C4-2B cells (mKO2 in red), cell nuclei [4′,6-diamidino-2-phenylindole (DAPI) in blue], and actin filaments (phalloidin in green). Asterisks (*) show hOBMT, full arrows show cancer cells, open arrows show scaffold fibers, full arrowheads show osteoblasts, and open arrowheads show a 70-μm-long cancer cell filopodia.

results showed that both enzalutamide and bicalutamide reduced the volumes of both LNCaP and C4-2B cells and decreased sphericity compared to the DHT control. This demonstrated the significant effect of antiandrogens in triggering an adaptive response. However, this effect was not as strong as compared to the drug-free control group. This allowed us to confirm our hypothesis that the efficacy of enzalutamide and bicalutamide in the presence of the bone microenvironment is compromised.

Reduced mineralization increases cancer cell migration

Cancer migration is an important parameter to evaluate metastatic activity and response to therapies. However, it is difficult to detect

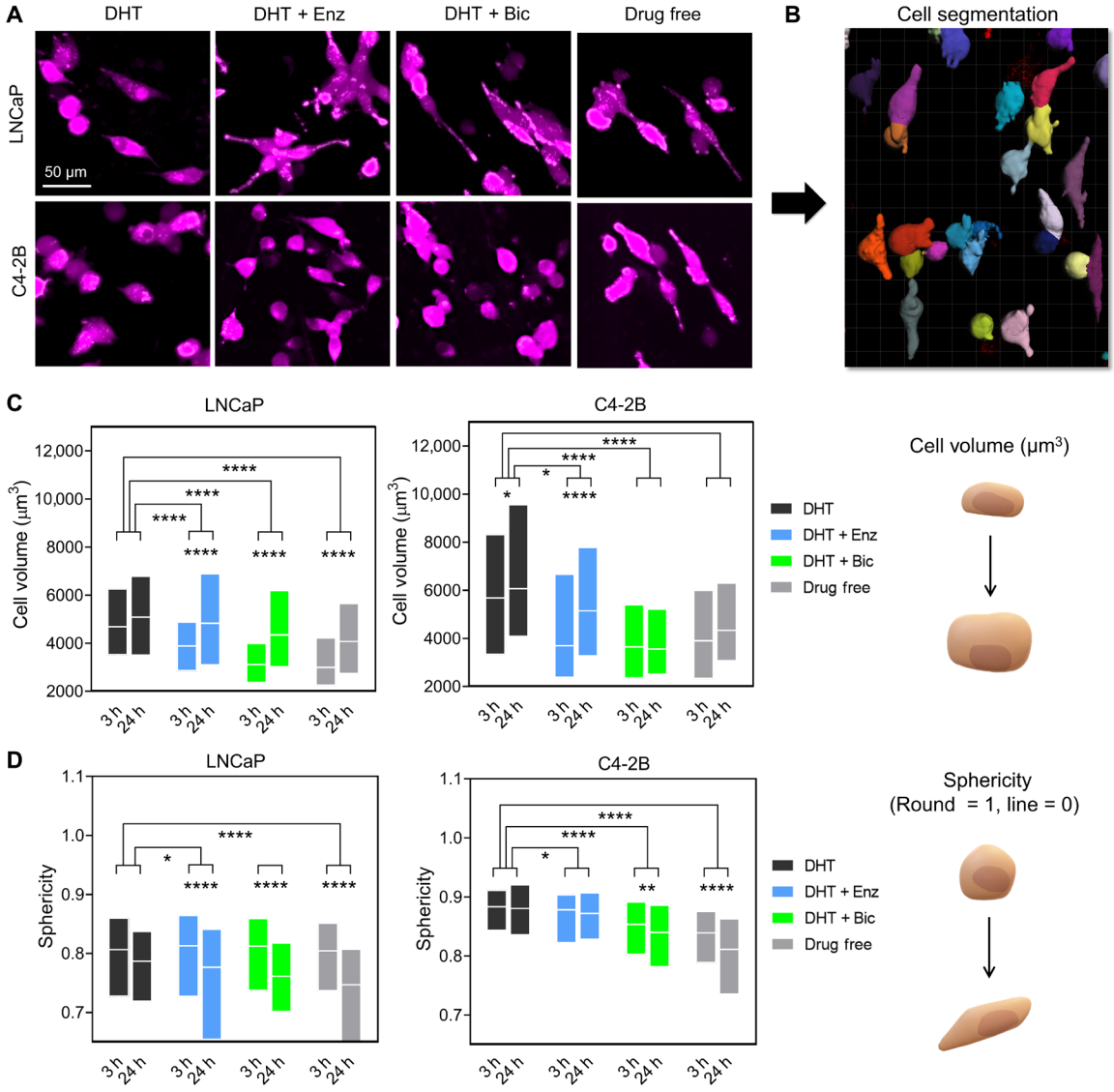

Fig. 2. Antiandrogen treatments increase cancer cell volume and reduces sphericity in the bone microenvironment. (**A**) Confocal microscopy images of the 3D metastatic microtissues after 24 hours hOBMT coculture with LNCaP and C4-2B under treatments, showing cancer cell morphology (mKO2) on hOBMT (MaxProj. shown, 70-μm z-stacks). (**B**) Cell segmentation processing through Imaris software. (**C** and **D**) 3D morphometric properties of cancer cells after 3 hours and after 24 hours coculture under treatments, shown as box plots, (C) cell volume, and (D) sphericity (>2 microtissues per condition analyzed with >4 random fields of view, average $n = 365$ cells). DHT (dihydrotestosterone), 10 nM; Enz (enzalutamide), 10 μM; Bic (bicalutamide), 10 μM. *$P < 0.05$, **$P < 0.01$, and ****$P < 0.0001$.

and quantify individual cell movement in both a "3D" context and a "coculture" context. Leveraging from our experience with high-throughput spinning disc confocal imaging and the Imaris software, we prepared a methodology to track a high number of tagged cancer cells up to 48 hours in the mineralized microenvironment (*20*). Before characterizing the effects of antiandrogen treatments, we assessed how the degree of mineralization of the bone-like hOBMT constructs would affect the migration of cancer cells, considering the high mineralization degree found clinically in osteoblastic bone metastases. We hypothesized that reduced mineralization would increase cancer cell migration. This is in line with the widely accepted fact that an initial osteolytic component (modeled here by reduced mineralization) is essential for the initiation and expansion of the osteosclerotic lesions. These lesions are subsequently dominating in 95% of all prostate cancer bone lesions (*21*). Varying the mineralization degree in the in vitro model was obtained by creating hOBMT constructs from isolated bone cells from three different male patients with various degree of mineralization. This was determined by alizarin red staining in 2D (patient 1 < 2 < 3) cultured for 8 weeks or by varying osteogenic culture time for one patient (8 < 12 weeks). As expected (Fig. 3, A and B), micro–computed tomography analysis showed more mineralization according to enhanced osteogenic capacity and longer culture time (*16*, *17*). Next, we preconditioned the mKO2-tagged LNCaP and C4-2B cells in DHT for 7 days before seeding on the various hOBMT constructs, similarly to the morphometry analysis, and assessed mean

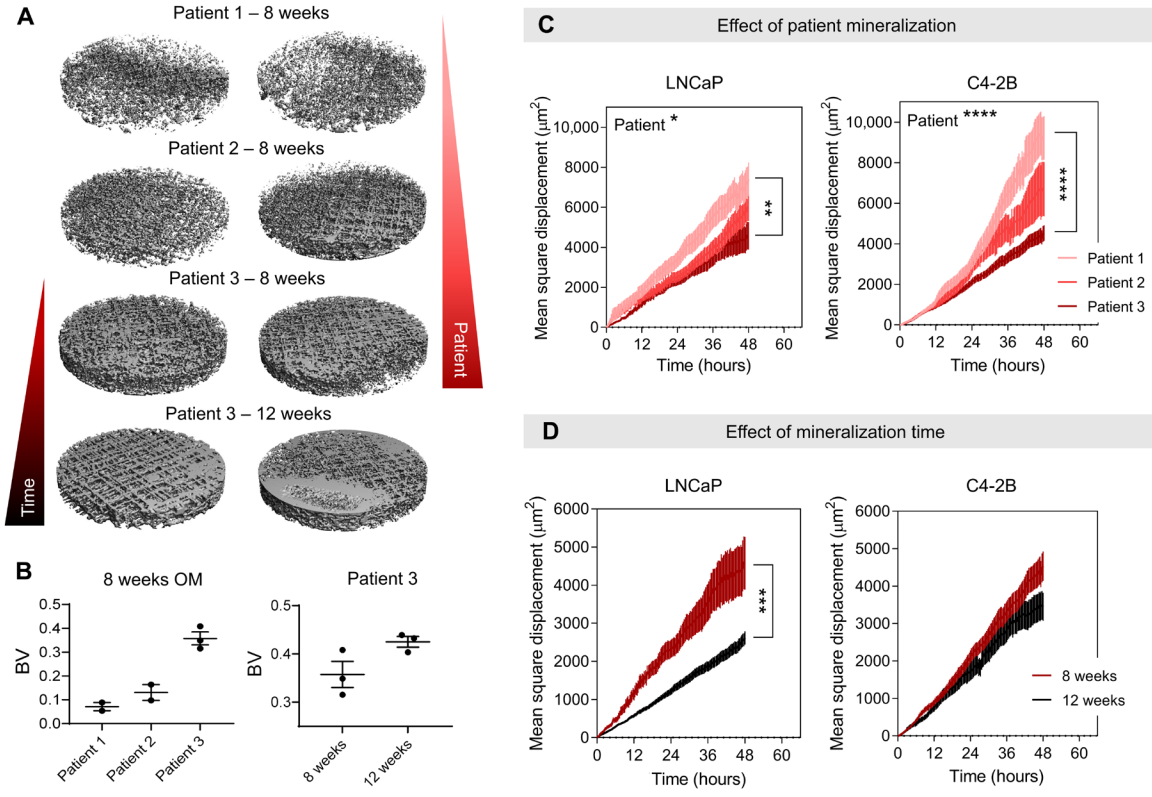

Fig. 3. Reduced mineralization increases cancer cell migration. (**A**) Micro–computed tomography images of 5-mm biopsy punches hOBMT before coculture with cancer cells and (**B**) corresponding mineralization volumes ("BV"). Means ± SE, $n = 3$. (**C** and **D**) Mean square displacement of LNCaP and C4-2B on hOBMT over 48 hours under 10 nM DHT, according to (C) patients with increasing mineralization capacity (1 < 2 < 3) shown for 8 weeks culture in osteogenic media and (D) culture times in osteogenic media shown for patient 3 (8 weeks versus 12 weeks). Over two microtissues per condition analyzed with >8 random fields of view, for average $n = 404$ tracks. Means ± SE. *$P < 0.05$, **$P < 0.01$, ***$P < 0.001$, and ****$P < 0.0001$.

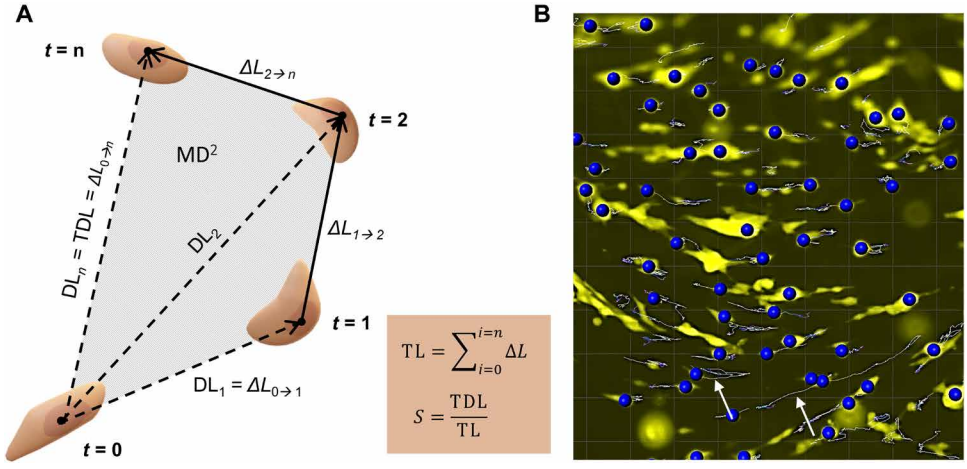

Fig. 4. Cancer cell migration on hOBMT constructs. (**A**) Schematic of cancer cell movements and associated parameters. t, time; DL, displacement length from $t = 0$; ΔL, displacement length from $t = n$-1 to $t = n$; TL, track length; TDL, track displacement length; S, straightness; MD^2, mean square displacement. (**B**) Imaris snapshot showing cancer cells (yellow) migrating on hOBMT (black) and resulting identified tracks (arrows).

square displacement for more than 400 cells per condition. Mean square displacement (or MD^2) represents the average area traveled by cancer cells on hOBMT over time per condition and is defined in square micrometers. It is represented in Fig. 4A, among other migratory parameters. An increase in mean square displacement correlates with increased cancer migration, a known hallmark in cancer metastasis. It thus represents a useful quantitative tool to assess cancer cell behavior in a specific microenvironment. It was

conclusively shown here in Fig. 3 (C and D) that reduction in mineralization led to increased cancer cell migration for both LNCaP and C4-2B cells, in accordance with the hypothesis. This result was observed either by the use of less mineralizing primary cells or reduced culture time in OM.

Antiandrogen treatments affect the short-term proliferation and migration of LNCaP cells, but not C4-2B cells, in the bone microenvironment

To analyze the effects of antiandrogens in the metastatic microtissues, hOBMT were made from the primary cells of one patient (patient 2) cultured for 8 weeks in OM, before coculture with cancer cells. Mineralization of the resulting hOBMT was shown previously in Fig. 3. The migratory analysis of cancer cells on hOBMT for 48 hours of coculture was performed for 8 to 16 random fields of view per microtissue, accounting for an approximate average of 700 cancer cell tracks analyzed per condition, thus giving a high statistical confidence in the results presented here. A snapshot of cell track identification by Imaris on one field of view from the live epifluorescence data is shown in Fig. 4B. In terms of quantitative parameters, next to mean square displacement (MD^2), other migratory parameters are helpful in getting a more comprehensive picture of cancer cell movement in the metastatic microtissues. These parameters are shown in Fig. 4A and include TDL (the total displacement length in micrometer), TL (the track length in micrometer), and *S* (the straightness, the ratio of TDL upon TL, indicative of cancer cell directionality) (*20*). Cancer cell *Speed* is another parameter that can be obtained by Imaris. Together, these parameters provide useful information on the activity of cancer cells within a defined microenvironment, for instance, whether cells travel extensively (higher MD^2, *TL*, and *TDL*) and actively follow a direction (*S* closer to 1) or remain relatively localized (*S* closer to 0). Together, these parameters, when high, relate to overall increased migration, a pivotal step in metastasis, associated with worse outcomes (*22*). Along with migration, proliferation is another indication of adverse progression and was measured here by fluorescence intensity over time.

After preconditioning of mKO2-LNCaP and C4-2B cells and coculture with the hOBMT constructs for 48 hours under various treatments, we proceeded to study the effects of enzalutamide and bicalutamide treatments on proliferation and migratory parameters in respect to both DHT and drug-free controls (Fig. 5). We hypothesized that the C4-2B cells on hOBMT would be less significantly

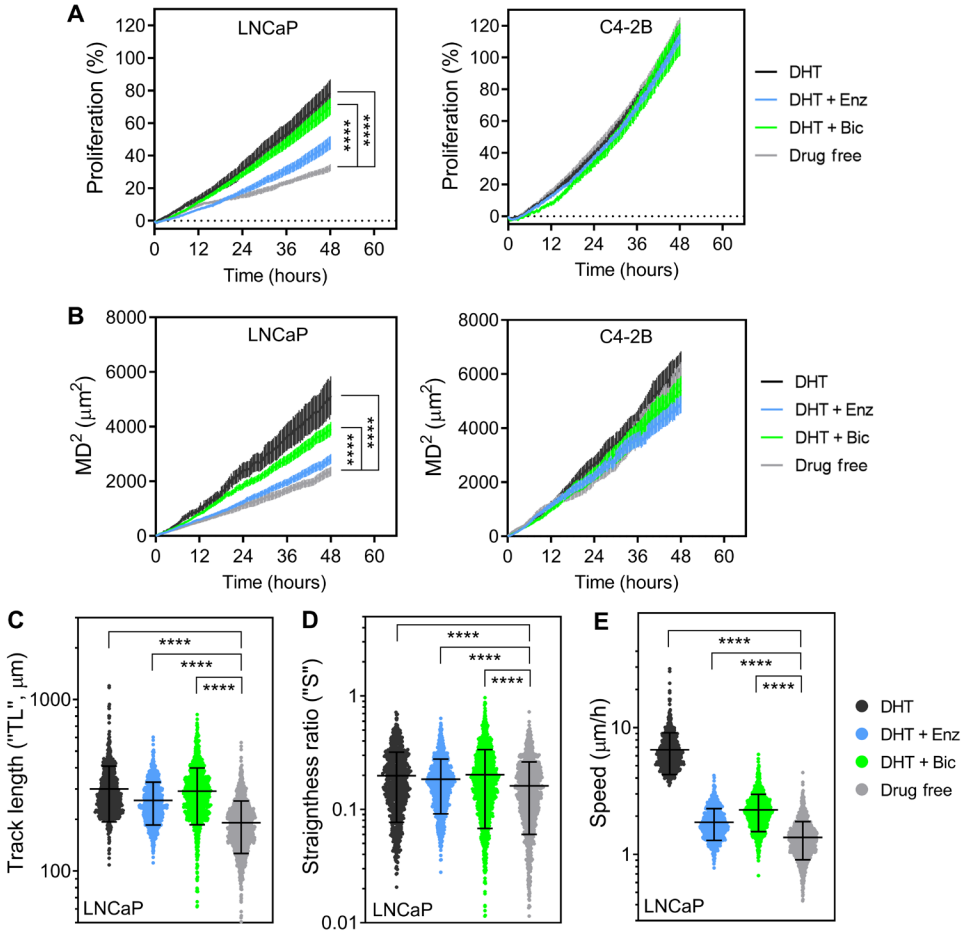

Fig. 5. Antiandrogen treatments affect the proliferation and migration of LNCaP but not C4-2B cells in the bone microenvironment. (**A**) Cancer cell proliferation and (**B** to **E**) migration properties of cancer cells on hOBMT over 48 hours under various drug treatments; (B) mean square displacement, (C) track length, (D) straightness ratio, and (E) average cell speed. Over two biologically independent microtissues per condition analyzed with >8 random fields of view, for average $n = 649$ tracks. Means ± SE shown for (C) to (D) and scatter plots with means ± SE shown for (E) to (G). DHT, 10 nM; Enz (enzalutamide), 10 µM; Bic (bicalutamide), 10 µM. ****$P < 0.0001$.

affected by the treatments, as being independent of androgens. We also hypothesized that the LNCaP cells would have the lowest outcome in the drug-free group, as being highly dependent on the androgens, especially at the early homing stage. These hypotheses were verified for proliferation, MD^2 and other migratory properties (Fig. 5 and fig. S1). In terms of antiandrogens, it is now widely accepted that enzalutamide is more effective than its predecessor bicalutamide, as shown in patients with CRPC (*5*). Thus, we expected higher efficiency at reducing cancer cell proliferation and migration with enzalutamide compared to bicalutamide but, again, only for LNCaP cells. The results from Fig. 5 and fig. S1 are in line with this hypothesis, where, overall, bicalutamide was less effective compared with enzalutamide at reducing the proliferation and migration of LNCaP cells on hOBMT, but no differences were observed for C4-2B cells. Yet, except for proliferation and total distance traveled (MD^2), where enzalutamide addition generated the same results as the drug-free controls (no statistical differences; Fig. 5, A and B), the other migratory parameters (*TL*, *S*, and *Speed*) were not equivalent to the drug-free control and statistically higher (Fig. 5, C to E). This suggests again support from the bone microenvironment in promoting LNCaP cell migration. This effect was even more strongly observed for bicalutamide, where all proliferation and migratory parameters were only slightly reduced and sometimes not even significantly compared to the DHT control. This further suggests an even stronger contribution of the bone tumor microenvironment in counteracting the effects of bicalutamide.

Antiandrogen treatments only slightly reduce the long-term proliferation of LNCaP micrometastases but have no effect on C4-2B micrometastases in the bone microenvironment

The previous methodology enabled to follow the proliferation and migration of cancer cells in the bone microtissues via imaging within a short timeframe (every 20 min). However, this could only be done over 48 hours due to the subsequent aggregation of cancer cells into micrometastases, rendering individual cell analysis impossible. Nevertheless, an asset of the metastatic microtissues is their macroscopic size (1 cm × 3 mm). This enabled to move the microtissues back to routine culture but conveniently collect them for localized fluorescence imaging and analysis at subsequent time points. This was done here at 7, 14, and 21 days coculture to assess the effects of antiandrogens on micrometastases with full mapping of the metastatic constructs (Fig. 6A and fig. S2) and subsequent image analysis (Fig. 6B). Here, it was shown, as could be anticipated, that DHT depletion led to overall decreased micrometastases growth for both LNCaP and C4-2B cells (2.2- and 2.8-fold, respectively) on hOBMT, compared to the DHT control. The drug-free groups had the lowest metastatic burden, with no growth for LNCaP micrometastases and 1.8-fold growth for C4-2B micrometastases. Higher-magnification images (Fig. 6C) showed that the morphology of aggregates was, however, similar, and differences between conditions were mostly seen in the "quantity" of micrometastases aggregates. Antiandrogen treatments in the LNCaP/hOBMT micrometastases followed similar trends as was seen during the 48-hour analysis yet showed that the Enz group was still higher than the drug-free control (1.41- versus 0.91-fold, $P < 0.05$), demonstrating growth of micrometastases under enzalutamide instead of metastases reduction. This effect was even stronger with Bic, which did not even reduce metastatic burden significantly compared to the DHT control [1.85- versus 2.2-fold, P = not significant (ns)]. For the C4-2B constructs, while no differences in proliferation was seen at 48 hours for treatments, the drug-free control became the lowest compared to all other groups after 3 weeks (1.86- versus 2.66- to 2.75-fold, $P < 0.0001$). Yet, the C4-2B growth under Enz and Bic was not reduced and similar to the DHT control (P = ns), confirming the inefficiency of both antiandrogen treatments to provide any reduction in metastatic burden for C4-2B cells in the bone microenvironment.

Metastatic microtissues display up-regulated *AR* and *ALPL* gene expression, which expression at the protein level was localized in cancer cells

We next looked at gene and protein expression in cocultures under enzalutamide and bicalutamide treatment. As controls, we used LNCaP cells and C4-2B cells or the hOBMT constructs cultured alone. As test groups, we used the LNCaP/hOBMT and C4-2B/hOBMT cocultures. We looked at prostate-specific antigen (*PSA*, also known as kallikrein-3 *KLK3)*, *AR*, bone-relevant genes, and EMT and NEtD genes, all relevant in osteoblastic metastases and prostate cancer cell adaptive response (Fig. 7A). Regardless of treatments, in general, the metastatic constructs presented a response midway between cancer cell controls and the hOBMT constructs. The exception was *AR*, which the metastatic constructs up-regulated significantly compared to individual controls, for both LNCaP/hOBMT and C4-2B/hOBMT constructs. This was shown in particular for LNCaP/hOBMT constructs, in line with stronger *AR* expression in LNCaP cells (Fig. 7A). Immunohistochemistry (IHC) showed that this increase in expression was exclusively localized in the cancer cells within the cancer cell/hOBMT cocultures (Fig. 7B), as very low AR was detected in the hOBMT. This observation was not affected by the coculture. The other important exception at the gene level in the metastatic constructs was alkaline phosphatase (*ALPL*), which, despite being lowly expressed in both individual cancer cells and hOBMT, was strongly expressed in C4-2B/hOBMT constructs (Fig. 7A). This correlated with the IHC with ALP protein expression increased in the cancer cells component of the metastatic constructs (Fig. 7B) in line with increased serum levels of bone-specific alkaline phosphatase seen in patients with metastatic prostate cancer (*23*).

Antiandrogen treatments failed to reduce PSA expression in the bone microenvironment and contributed to increased bone production/maturation and NEtD markers

As expected with antiandrogens, PSA was decreased in single cancer cell cultures, to a stronger extent in LNCaP than C4-2B, while not expressed at all in hOBMT. Yet, in cocultures, PSA expression was either slightly increased (gene level; Fig. 7A) or similar (protein level; Fig. 7C) when enzalutamide and bicalutamide were administered, as seen at both gene and protein levels. This showed a direct contribution from the bone microenvironment to maintain PSA expression. Subsequently, although nonsignificant for *ALPL*, we observed increased expression of a variety of bone-related markers to a stronger extent in LNCaP/hOBMT constructs compared to C4-2B/hOBMT constructs (Fig. 7D). This included members of the small integrin–binding ligand *N*-linked glycoproteins, namely, *IBSP* and osteopontin (*OPN*, also known as *SPP1*), and the transcription factor *RUNX2*, expressed usually in maturing osteoblasts. Inhibitors of *Wnt* signaling, namely, *DKK-1* and *SOST*, were also overexpressed strongly, the latter in line with circulating sclerostin levels significantly increased in patients receiving antiandrogen therapy (*24*). *DDC*, a NEtD marker playing a key role in castrate resistance progression

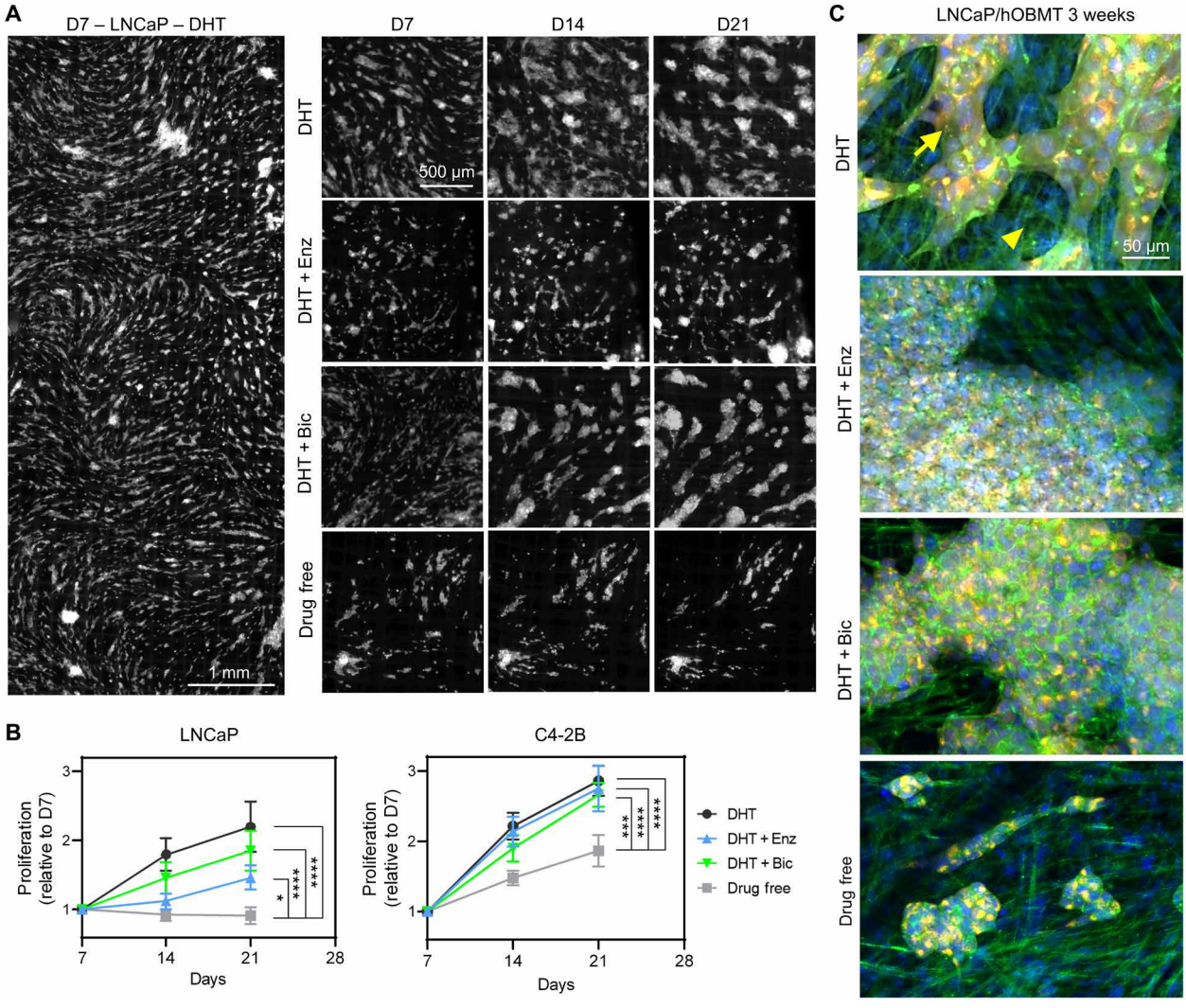

Fig. 6. Antiandrogen treatments only slightly reduce the long-term proliferation of LNCaP micrometastases but have no effect on C4-2B micrometastases in the bone microenvironment. (**A**) Epifluorescence images of LNCaP/hOBMT metastatic constructs up to 21 days for various treatments (mKO2 channel shown). (**B**) LNCaP and C4-2B proliferation on hOBMT, up to 21 days, normalized to the area of cancer cells on hOBMT at day 7 (D7), $n = 4$ to 5, means ± SE shown. (**C**) Confocal microscopy images of metastatic microtissues after 21 days coculture under various treatments [DHT, 10 nM; Enz (enzalutamide), 10 µM; Bic (bicalutamide), 10 µM], showing merged images from DAPI (blue), phalloidin (green), and cancer cells (mKO2, red). Full arrows show cancer cells. Arrowheads show osteoblasts (MaxProj. shown, 70-µm z-stacks). *$P < 0.05$, ***$P < 0.001$, and ****$P < 0.0001$.

(*25*), was strongly up-regulated in both types of metastatic constructs, under antiandrogen therapies (844-fold for DHT + Enz and 471-fold for Bic, compared to DHT alone), showing strong adaptive response from cancer cells under antiandrogen treatment in the bone microenvironment.

DPP4 and RBP4 were found expressed in both types of metastatic constructs, compared with LNCaP, C4-2B, or hOBMT alone

Next to the changes in bone and NEtD markers, wider protein arrays (119 various cytokines screened; figs. S3 and S4) revealed that dipeptidylpeptidase 4 (DPP4), known to be involved in cell-ECM interactions, was expressed in both metastatic constructs compared to respective monocultures (Fig. 7E and fig. S5). This was further validated at the gene level with reverse transcription quantitative polymerase chain reaction (RT-qPCR), with a 10-fold increase under enzalutamide and 5-fold increase under bicalutamide (Fig. 7A) compared to DHT only. It was also confirmed via IHC that while DPP4 was observed in both cancer cells and hOBMT, the metastatic constructs resulted in increased DPP4 staining in cancer cells, which was stronger in C4-2B/hOBMT constructs. This is in line with increased expression detected by protein arrays (Fig. 7E). Last, retinol-binding protein 4 (RBP4), an adipokine involved in insulin resistance, which was either not detected at gene or protein level in LNCaP or C4-2B monocultures or at low levels in hOBMT, was found expressed by cancer cells and the lining cells in hOBMT in the metastatic constructs, particularly in LNCaP/hOBMT constructs (Fig. 7F and fig. S5). This was further validated with RT-qPCR, which also

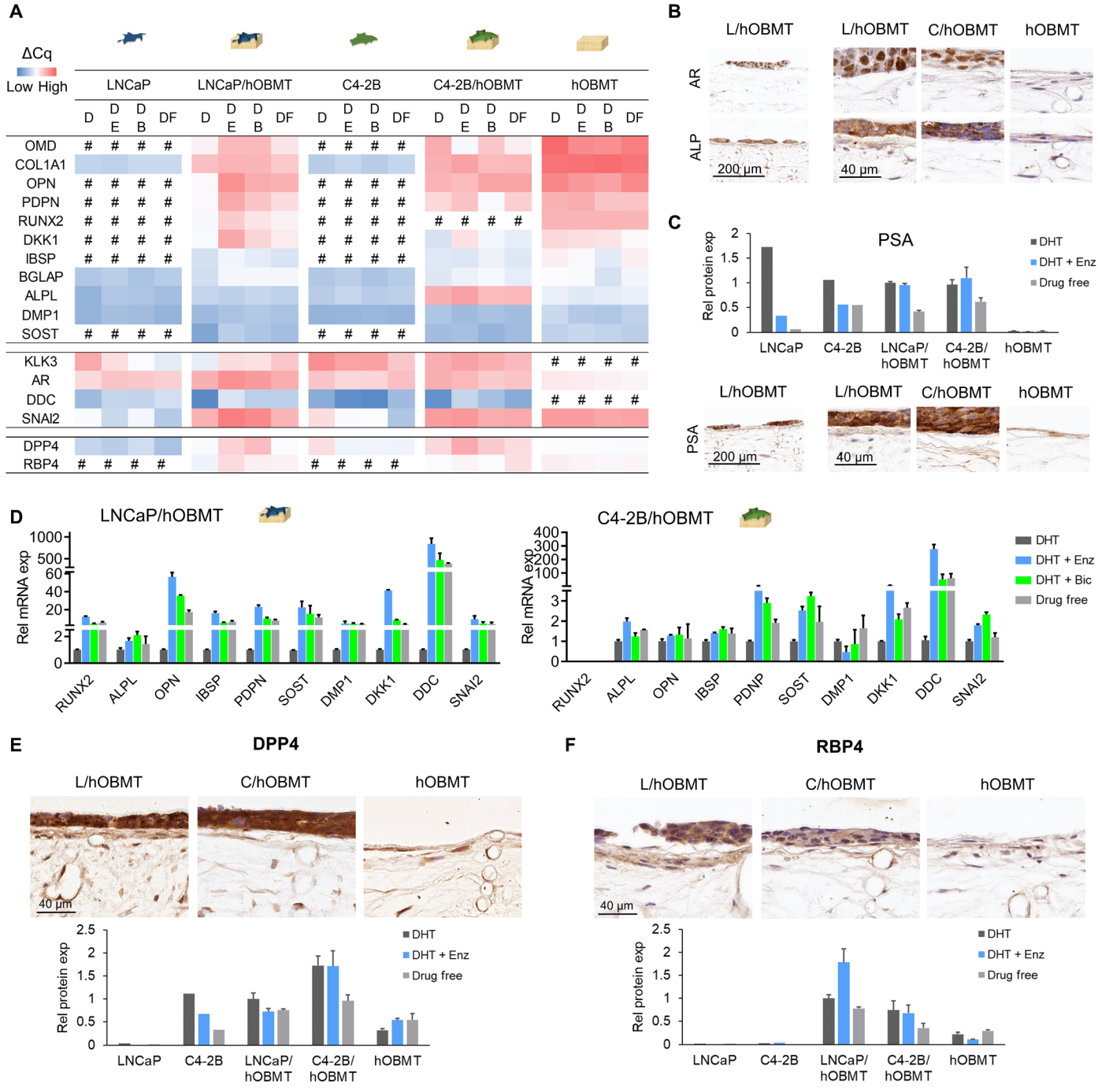

Fig. 7. Cocultures and antiandrogen treatments dysregulate bone microenvironment markers. (**A**) Heatmap of mean ΔCq values from RT-qPCR analysis of LNCaP, C4-2B and hOBMT monocultures, and LNCaP/hOBMT and C4-2B/hOBMT constructs. D, 10 nM DHT; DE, 10 nM DHT +10 μM enzalutamide; DB, 10 nM DHT +10 μM bicalutamide; DF, drug free. (**B**) IHC images showing AR and alkaline phosphatase (ALP) expression in hOBMT monocultures and metastatic constructs under DE treatment. (**C**) Prostate-specific antigen (PSA) expression measured from conditioned media and microarray membranes (top; means ± SD, $N = 2$ patients) and IHC images (bottom), the latter under DE treatment. (**D**) Relative mRNA expression of metastatic constructs under treatments, normalized to DHT for each gene of interest. $N = 3$, means ± SE. (**E** and **F**) IHC images (top) and protein expression from microarray membranes (bottom; means ± SD, $N = 2$ patients) of dipeptidyl peptidase 4 (DPP4) (E) and retinol-binding protein 4 (RBP4) (F) under DE treatment. L, LNCaP; C, C4-2B.

showed a 12-fold increase under enzalutamide and 5-fold increase under bicalutamide (Fig. 7A) compared to DHT only, in the metastatic constructs. Those results suggest synergistic effects of cancer cells, the bone microenvironment, and antiandrogens to activate previously unidentified interesting targets.

DISCUSSION

While prostate cancer metastatic lesions are the result of dysregulated activities of osteoclasts and osteoblasts, osteoblasts remain the key drivers in prostate cancer progression. Radiological evidence indeed shows osteoblastic lesions found located near osteoblast areas (*6*) and thus rationalizes an osteoclast-free approach in the first instance, as also highlighted by others (*13*).

Various models of bone metastasis/metastases have emerged in the past few decades, targeting different aspects of bone metastasis. They include 2D Transwell cocultures, multicellular spheroids (scaffold-free) (*26*), cell-encapsulated bioprinted/engineered matrices (scaffold-based) (*27*, *28*), and ex vivo cultures (*29*) and can be used in static or dynamic modes (*13*). While every model comes with its pros and cons, only a few models have been used to answer relevant biological questions, such as assessing the effects of current or new drugs in the bone tumor microenvironment. An exception is the work by Fong *et al.* (*27*), where inhibition of FGFR1 using dovitinib replicated some of the results of a clinical trial showing efficacy of this drug in mCPRC patients with reduced bone lesions. Two limitations of this model are, however, the use of a mouse osteoblast cell line and the lack of a mineralized matrix. Here, we have used a microtissue-engineered osteoblastic in vitro human model. It was made of primary human osteoprogenitors differentiated in early and mature osteoblasts and osteocytes and matrix biomineralization, for direct interactions with prostate cancer cells (*16*). We applied the model to the study of the antiandrogens, bicalutamide, and enzalutamide, recapitulating the local microenvironment of most patients with advanced mCPRC under such treatment and that have progressed to the bone. The strengths of this model are its high reproducibility via melt electrowriting manufacture, its all-human cell components with cell-cell and cell-matrix direct contacts, its osteoblast/osteocyte populations, its high and controllable degree of mineralization, and its long-term cell viability. When cocultured with prostate cancer cells, the "metastatic model" is amenable to the rapid analysis of a high number of individual cancer cells, in terms of migration, proliferation, and 3D morphometry, as well as micrometastases growth overtime (*16*, *30*, *31*).

In prostate cancer, the reactivation of the transcription factor AR is pivotal to progression toward CRPC, taking place, on average, within 2 to 3 years after testosterone suppression (*7*). It is now indeed accepted that most metastatic CRPC are driven by a transcriptionally active AR, despite castrate levels of circulating androgens (*5*), with amplification, mutation, and splice variants, the common alterations that remain drivers of castrate-resistant disease progression (*32*). In response, the discovery of an entity that could bind the ligand-binding pockets of AR was a significant achievement in the treatment of prostate cancer, as it enabled the prevention of androgen binding to AR by competitive inhibitors (*5*). As a result, two treatment strategies have since prevailed: the use of first-generation antiandrogens, nonsteroidal (e.g., flutamide, nilutamide, and bicalutamide), and the use of second-generation antiandrogens, which prevent androgen synthesis (e.g., CYP17 inhibitor, abiraterone acetate, and MDV3100, known as enzalutamide). Various clinical trials have studied these drugs alone and in combination, and it has appeared that second-generation antiandrogens are more successful in improving overall patient survival (*33*). For instance, enzalutamide has from five- to eight-time better affinity for AR than bicalutamide and does not have an agonistic effect on the transcriptional activity of AR (*5*). Enzalutamide may often be used after docetaxel chemotherapy, leading to over 50% reduction in PSA serum levels in patients, as shown via the AFFIRM clinical trial. It was also shown to bring a 78% PSA reduction in chemonaïve patients (enzalutamide alone, no docetaxel) via the PREVAIL clinical trial, currently rationalizing enzalutamide alone or in combination as the standard of care in mCRPC treatment (*34*).

Yet, a majority of enzalutamide-treated patients with initially a strong decline in serum PSA levels eventually see PSA levels rising again and/or progression in the bone, suggesting acquired resistance (*10*). Androgens are critical to bone health and function and are strongly mediated by the estrogen receptor and AR, where they serve to maintain cancellous bone mass, expand cortical bone, and protect men against osteoporosis (*35*). Androgen deprivation therapy is thus associated with an overall detrimental effect on bone health, with reduced bone mineral density (BMD) and bone fragility (*2*), although enzalutamide and bicalutamide had initially not shown the same reduction in BMD (*36*). Yet, Armstrong *et al.* (*37*) recently published a secondary analysis of the PREVAIL and AFFIRM randomized clinical trials, which showed a different picture. Certain men responding to enzalutamide show new unconfirmed bone lesions detected at posttreatment scintigraphy, which has been interpreted as an osteoblastic reaction representing healing. Yet, the secondary analysis revealed that the detection of these lesions in mCRPC men that responded to treatment with enzalutamide after docetaxel appeared to be associated with worse overall survival and may represent true progression (*37*). Such ambivalent pictures highlight the need for advanced models that better represent the clinical and therapeutic context to understand whether and how endocrine alterations in this microenvironment contribute to cancer progression, so that clinical outcomes can be improved (*2*, *36*).

Using the model developed here, it was shown that AR signaling was increased under antiandrogens in the metastatic constructs and that the increase was localized in cancer cells (not seen in the bone cells) and more strongly for AR-responsive cells. This is in line with AR reactivation under antiandrogens at the onset of adaptive response (*38*) and in line with enzalutamide-treated patients having increased nuclear AR in the bone tumor microenvironment (*39*). There was an increase of such signaling in cancer cells in the metastatic constructs (to a higher extent in LNCaP/hOBMT constructs), even before antiandrogen administration. This suggests that cancer/bone stroma interactions take a part in amplifying AR, further leading to the activation of AR-related pathways and responses in this microenvironment (*36*). Such adaptive responses were first seen morphologically through the stronger LNCaP phenotypic adaptations observed via morphometric analysis as early as 3 hours after coculture. Programs such as NEtD and EMT are indeed controlled by pseudopodial actin dynamics, with cancer cells displaying morphological features representative of adaptive response (*18*, *19*). They represent useful tools when they can be quantified, which was done in 3D via the methodologies developed here. It was observed that LNCaP cancer cells had a reduced sphericity when cocultured with the hOBMT, further strengthened by antiandrogen administration. This was correlated by the strong expression of *DDC*, a NEtD marker and AR

coactivator acting at the cytoplasmic level, centrally involved in castrate resistant progression (*25*).

The bone-like microenvironment overall showed active participation to maintaining the growth and adaptive response of cancer cells, even before antiandrogen administration. This was seen with initial androgen suppression in media, which is mimicking the earlier clinical step with androgen ablation treatments. There was an increase of cancer cell volume within the first 24 hours of coculture with hOBMT, due to the abundance of GFs derived from the bone-like microenvironment (*40*). Several markers of osteoblast differentiation (*RUNX2*), ECM deposition/mineralization (*BGLAP*, *OPN*, *IBSP*, and *ALPL*), and maturation into preosteocytes (*PDPN*, also known as *E11*, *DMP1*, and *SOST*) were overexpressed when androgens were removed. This is in line with previous work (*16*), leading to cancer cell osteomimicry, with increased osteoblastic activity, which is correlated with lesions seen in the radiological data of men with bone mCPCR (*6*) and through serum markers. For instance, alkaline phosphatase (ALP) serum levels are indeed elevated in mCPRC (*23*) and *BGLAP*, and *IBSP* promoter activities are typically increased in LNCaP and C4-2B 2D cocultures with bone stromal cells (*41*). Here, we showed that this process of osteomimicry contributed to cancer cell survival in the bone microenvironment, whether antiandrogens treatment had been used or not. This effect was further accentuated by androgen removal, which is mostly the case in patients, before being treated with antiandrogens as the next clinical treatment option.

The further use of bicalutamide or enzalutamide on the metastatic constructs showed, in general, that except for increased *DDC* expression in C4-2B cocultures under Enz/Bic, and in line with more elongated phenotypes seen by morphometry, C4-2B/hOBMT under Enz/Bic were not or little affected at proliferation, migration, and gene and protein levels. This none-to-minimal effect of antiandrogens is in line with their AR independence as C4-2B cells are derived from a bone metastasis past transition to castrate resistance (*42*). Therefore, these cells are able to grow in the androgen-deprived bone microenvironment and are minimally affected by antiandrogens. Conversely, the AR-dependent LNCaP cells, derived from a lymph node metastasis, had a response, albeit limited, to antiandrogens, showing support from the bone microenvironment. The choice of such cell lines to further study adaptive response mechanisms is highly relevant as it represents the two groups of patients with bone mCPRC, with one group already resistant to androgen deprivation with no benefit from further suppressing AR signaling and another group where AR signaling remains meaningful, although not the only driver (*32*), enabling to further assess potential mechanisms of transition toward castrate resistance.

The use of bicalutamide or enzalutamide on the metastatic constructs with LNCaP revealed that antiandrogens contributed to some reduction in cancer cell migration and proliferation in the microenvironment, yet the latter alarmingly maintained up to 3 weeks, whereas the drug-free control showed no proliferation. The maintenance of PSA in this microenvironment supported such proliferation and may be a direct consequence of osteoblast-secreted factors that cause independent induction of PSA through AR-related mechanisms (*43*) or decrease in antiandrogen efficacy in the microenvironment. It was shown that most bone differentiation and maturation markers were indeed up-regulated with enzalutamide, in particular for *OPN*, *PDPN*, *SOST*, *IBSP*, and *RUNX2*. The up-regulation of *SOST* in LNCaP/hOBMT constructs is in line with circulating sclerostin levels significantly higher in patients receiving antiandrogen therapies (*24*). Yet, SOST expression led to lower rates of metastasis (*44*), which explained the reduced migration of LNCaP cells in LNCaP/hOBMT constructs under Enz/Bic and the unaffected migration in C4-2B/hOBMT constructs. The expression of PSA in the bone microenvironment may be a better indicator than systemic PSA assessment for mCPRC progression, as it is known that systematic PSA decrease is not representative of local active PSA in bone, which is more expressed in well-differentiated local tumors (*45*), although systematic PSA is low. This is also confirming that the effects of antiandrogens on bone scans are inconsistent with favorable systemic PSA response, where patients progress despite an initial systemic PSA decrease. This effect was also reported using a patient-derived xenograft (PDX) model of bone mCPRC (Prostate Cancer San Diego 1). When the PDX was implanted subcutaneously and treated with Bic, the tumor reduced significantly (*46*). However, Bic was ineffective when implanted intrafemorally in mice, although PSA was systemically reduced (*46*). A similar PSA reduction was observed when the former PDX tumor cells were implanted intrafemorally as patient-derived organoids and treated with Enz; Enz did not reduce overall viability, although PSA was misleadingly reduced systemically (*47*). These are important studies that corroborate our own findings with this platform.

Using our model, we were also able to observe the limited effects of enzalutamide and bicalutamide on cancer cells in the osteoblastic microenvironment. We noted that bicalutamide was less effective than enzalutamide, as expected through its partial AR agonistic activity absent when using enzalutamide (*5*), and seen in LNCaP and C42B due to the AR mutation T877A (*48*). Yet, we learned that enzalutamide administration, although more effective on overall migration and proliferation of AR-dependent LNCaP cells in the bone microenvironment compared to bicalutamide, led to more bone microenvironment gene alterations (*OPN*, *E11*, *RUNX2*, *BSP*, and *DKK1*) than bicalutamide, although no significant differences were observed in *AR* expression between both drugs. This implies that the effects of enzalutamide triggered more response than bicalutamide at the level of cancer/bone stroma interactions and with less dependence on *AR* expression. *DKK1*, in particular, was the marker most up-regulated under Enz (five times more compared to Bic). *DKK1* is expressed by osteocytes, an asset of the hOBMT construct, and is also involved in the initiation of osteoblastic prostate cancer metastasis, by altering cancer cell phenotype and neighboring bone stroma. DKK1 specifically stimulates osteoclastogenesis, which is responsible for further release of GFs and fueling the osteoblastic lesions (*49*). It may thus be concluded that the use of enzalutamide in the bone microenvironment may lead to stronger adaptive responses and osteomimicry than bicalutamide, although presenting with better cancer reduction through functional analysis (proliferation and migration). This is in line with enzalutamide delaying time to skeletal-related events and extending survival in mCRPC, although ultimately still failing patients (*1*).

As bone is a complex niche rich of GFs and other cytokines that may contribute to antiandrogen resistance (*50*), we used our model to screen for previously unidentified potential agents that may facilitate cancer progression. It is already known, for example, that the mineralized ECM of bone contains high levels of stromal cell–derived factor 1, which attracts cancer cells via C-X-C chemokine receptor type 4 (CXCR4) (*50*). AR signaling can also promote the cleavage of fractalkine from bone, further attracting prostate cancer cells

bearing CX3CR1 (*50*). Here, we report two interesting targets, DPP4 and RBP4, that were found not/lowly expressed in individual cancer cells or hOBMT yet were up-regulated in coculture and, to a higher extent, under antiandrogens. DPP4 is already known to be elevated in primary disease (*51*), and men under DPP4 inhibition had improved survival, although the mechanisms remain to be elucidated (*52*). Here, it was shown that DPP4 was also expressed in the bone tumor microenvironment, suggesting that inhibition of DPP4 for men with bone metastatic disease may also be relevant. Next, RBP4 is usually an adipokine that drives the development of insulin resistance and type II diabetes in patients with obesity. It was, however, shown previously that RBP4 promoted ovarian cancer cell migration and proliferation via the RhoA/Rock1 and ERK pathways and that it was increased in patients with ovarian cancer, presenting a useful serum marker (*53*). In prostate cancer, knockdown of RBP4 inhibited the growth of PC3 cells in vitro (*54*). Critically, the overexpression of RBP4 in murine preosteoblast cells (MC3T3-E1) cells promoted proliferation, differentiation, and mineralization of MC3T3-E1 with phenotype and markers expressed similar to the ones up-regulated in our model, including *RUNX2*, *BGLAP* (also known as *OCN*), and *OPN* (*40*), critical in osteogenesis. Many patients with prostate cancer are affected by metabolic syndrome, including insulin resistance and type II diabetes. It is likely that RBP4 may be overexpressed even before metastasis progression or antiandrogen administration, which may then be further expressed when the latter two happen. In turn, this may trigger the typical osteo-phenotypic response seen in osteoblastic lesions and thus represent an interesting target that needs to be further explored.

Overall, the microtissue-engineered in vitro 3D model and quantitative methodologies herein present an original model to investigate the interactions between primary human osteogenic cells and cancer cells and the effects of antiandrogen treatments, particularly depicting enzalutamide resistance, as seen in the clinical scenario. However, value will be gained from adding osteoclasts to the model, which likely also contribute to this cross-talk, via the OPG/RANKL/RANK pathway and secreted metalloproteinases. Yet, the benefit of having a mineralized microtissue tissue engineered from a single bone cell type is still important, enabling to decouple the roles of osteoblasts and osteoclasts in bone mCPRC. Osteoclasts are indeed often considered responsible for the initiation of the vicious cycle of metastasis by releasing factors that inducing stem cell osteogenic differentiation (*4*) and osteoblast activation (*11*). However, as stated by Ark *et al.*, (*10*) it is not currently known whether and how osteoclasts or osteoblasts affect enzalutamide resistance and whether the effects of enzalutamide on those cells contribute to drug resistance (*10*). Here, it was shown that the presence of osteoclasts was not necessary to activate such pathways. These pathways were (i) activated by direct interactions between human osteoblasts and cancer cells and (ii) accentuated by bicalutamide and enzalutamide, with worse outcome with bicalutamide yet stronger genomic dysregulation using enzalutamide in this microenvironment. Such findings may tentatively answer Ark *et al.*'s key question as to whether combining enzalutamide with approaches that also target osteoblasts and/or osteoclasts would lead to better therapies. With current focus on blocking osteoclast activities (e.g., through zoledronic acid or denosumab), yet with only palliative effects, our study demonstrates that it may be useful to simultaneously focus on osteoblasts as another valid source of antiandrogen resistance in mCRPC.

MATERIALS AND METHODS

Manufacturing of hOBMT

The hOBMT was prepared according to established protocols (*16*, *30*). Briefly, medical-grade polycaprolactone (mPCL) microfiber scaffolds (10 mm by 10 mm, 150-μm pore size, and 600-μm thickness) were printed via melt electrowriting using a custom in-house built apparatus (QUT, Brisbane, Australia). The resulting 3D porous scaffolds were coated with calcium phosphate (CaP) (*30*) before seeding with osteoprogenitor cells from healthy donor bone tissue (n = 3 male donors), collected in accordance with QUT ethics approval number 1400001024. Isolated cells were seeded at passages 3 and 4 on ethanol/ultraviolet-sterilized CaP-coated scaffolds (0.4×10^6 cells per scaffold) and differentiated osteogenically for 8 or 12 weeks (*16*, *30*) using alpha-Minimum Essential Medium α-(MEM) with ribonucleosides, deoxyribonucleosides, L-glutamine, phenol red, 10% fetal bovine serum (FBS), and 1% penicillin/streptomycin (P/S; 10,000 U/ml stock solution), all from Gibco, Australia, including 10 mM β-glycerophosphate, 0.17 mM ascorbic acid, and 100 nM dexamethasone, all from Sigma-Aldrich, Australia, with media changes every 3 to 4 days.

Micro–computed tomography

The resulting mineralized 3D microtissues were also analyzed using micro–computed tomography (μCT40, Scanco Medical, Brütisellen, Switzerland). The samples were scanned in phosphate-buffered saline with an isotropic voxel size of 6 μm^3 at 45 kV, 177 μA, and 300-ms integration time with four times averaging, resulting in 1.2-s sample time. The mineralization was evaluated by applying the same volume of interest (VOI) to all samples, by selecting the same circular region of interest with a diameter of 2.7 mm to a stack of 53 slices resulting in a VOI of 1.79 mm^3. The grayscale images were then segmented with a lower threshold of 140 (minimum/maximum: 0/1000), which was chosen by histogram analysis to separate mineralization from background noise. The settings were kept constant for all samples, and the resulting mineralization in (mg HA/ccm) was calculated with SCANCO's proprietary algorithms. The 3D reconstructions of the mineralized samples for each patient group are shown in Fig. 3.

Prostate cancer cell lines

Mycoplasma-free and Short Tandem Repeat analysis (STR)-profiled LNCaP and C4-2B (passages 22 to 34) from American Type Culture Collection were transduced with a pLEX307-mKO2 plasmid (donated by S.-A. Stephenson, QUT) and cultured in RPMI 1640 medium containing L-glutamine, 10% FBS, and 1% P/S and no phenol red, all from Gibco. Before coculture with hOBMT, cancer cells were preconditioned for 7 days in "drug-free" media, consisting of RPMI, 10% charcoal-stripped serum (CSS), 1% P/S, and vehicle controls; or "DHT" media, consisting of RPMI, 10% CSS, 1% P/S, and 10 nM DHT (Sigma-Aldrich diluted in 100% ethanol); or "DHT + Enz" media, consisting of RPMI, 10% CSS, 1% P/S, 10 nM DHT, and 10 μM enzalutamide (Selleck Chemicals, diluted in 100% ethanol); or "DHT + Bic" media, consisting of RPMI, 10% CSS, 1% P/S, 10 nM DHT, and 10 μM bicalutamide (Selleck Chemicals, diluted in dimethyl sulfoxide).

hOBMT coculture with prostate cancer cell lines

Preconditioned cancer cell suspensions were prepared at 1×10^5 cells/ml. The hOBMT, after 8 weeks of culture in osteogenic media, were cut in three equal stripes (3 mm by 10 mm) and placed in drug-free media for 24 hours in 1% agar-coated 24-well plates. Next, the

hOBMT were supplemented with 500 µl of the preconditioned cancer cell suspensions. After 24 hours of coculture on a rocking platform mixer (RPM4, Ratek Laboratory Equipment), supernatants were collected and hOBMT gently washed three times before further coculture in the corresponding media. Cancer cell attachment was determined by measuring the average cell concentration in collected supernatants, corrected from control wells (cancer cells only, no hOBMT).

Cancer cell morphometry

Metastatic microtissues were fixed in 4% paraformaldehyde (PFA; Sigma-Aldrich) for 40 min, after either 3 or 24 hours of coculture in the various conditions. SDC microscopy (X-1 Yokogawa with Borealis modification), fitted with a 10× Plan Apo objective and a red channel filter set (excitation 561 nm), was used to collect z-stacks of the coculture microtissues. Maximal intensity projections were made from z-stacks using 1 µm as the step size and 70 µm as the thickness (>2 microtissues per condition analyzed with >4 fields of view, for 365 cells analyzed per condition on average). Cancer cell volume and sphericity were obtained from Imaris imaging analysis software (version 9.1.0, Bitplane AG, Zurich, Switzerland) according to the algorithm of (*16*).

Live cancer cell imaging and analysis

After attachment, a fraction of metastatic microtissues were placed in a new 24-well plate and secured down using Teflon ring inserts (Prestige Manufacturing Pty Ltd.) (*31*). A live-cell inverted epifluorescence microscope (IX81,Olympus) fitted with a humidified chamber, 95% air, and 5% CO_2, set at 37°C, was used to collect images every 20 min for 48 hours. Fluorescent signals from mKO2-labeled LNCaP and C4-2B cells were used to track migration on the hOBMT. Analysis (mean square displacement, cellular speed, track length, and straightness) was performed using Imaris (parameters: estimated cell diameter, 18 µm; intensity filter, 30 to 230; max distance jumps, 20 µm; max gap size, 5) and proliferation analysis with ImageJ (1.51j8., National Institutes of Health, USA; parameters: Gaussian blur: 2, Huang thresholding). Two microtissues per condition were analyzed with ~8 fields of view per microtissue, for ~404 and ~649 tracks analyzed per condition, on average, for migration for Figs. 3 and 5, respectively.

Long-term proliferation and morphology

Metastatic constructs were grown in their respective media for 3 weeks. Every 7 days, fluorescence images of cancer cell colonization on hOBMT were taken of each condition using an inverted epifluorescence microscope (IX73 Olympus) set on the red channel filter set (excitation 561 nm). Cancer cell proliferation at 7, 14, and 21 days were measured using ImageJ, as mentioned above. After 21 days, the metastatic microtissues were fixed in 4% PFA for 40 min and stained for 4′,6-diamidino-2-phenylindole (DAPI) (5 µg/ml; Sigma-Aldrich) and fluorescein isothiocyanate–conjugated Phalloidin (200 U/ml; Sigma-Aldrich) for 1 hour and imaged by SDC microscopy (Plan Fluo ELWD 20× DIC objective) using green (excitation 488 nm), blue (excitation 405 nm), and red (excitation 561 nm) filter sets. Maximal intensity projections were made from z-stacks using 1 µm as the step size and 70-µm thickness (n = 4 to 5).

Gene analysis

RT-qPCR was performed on the PCa/hOBMT cocultures after 10 days coculture with either LNCaP or C4-2B under various drug treatments and compared with monocultures, cultured in the same conditions. This time point was chosen to ensure similar ratios between bone and cancer cells so that comparison between conditions could be performed. At collection point, RNA was collected and extracted, reverse-transcribed, and processed for RT-qPCR to interrogate osteogenic, NEtD, EMT, and other relevant gene expression. Briefly, samples first were collected in TRIzol reagent (Invitrogen) for RT-qPCR analysis. After RNA isolation using Direct-zol RNA MiniPrep (Zymo Research, Australia), 440 ng of RNA was reverse-transcribed with the SensiFAST cDNA Synthesis Kit (Bioline, Australia), as per the manufacturer's protocol, and RT-qPCR was performed using the SYBR Green PCR master mix (Thermo Fisher Scientific) on a QuantStudio 5 system (Applied Biosystems). Amplification conditions were 95.0°C for 10 min, 40 cycles of 95°C for 15 s, and 60°C for 1 min. Amplification specificity was verified by melting curve analysis. Expression of target mRNA was determined using the delta-delta Cq method, using *MRPL42* and *RPL32* gene expression, geometrically averaged, as reference genes. The following primers were purchased from Sigma-Aldrich: osteomodullin (*OMD*; forward: TCCTGGTTTGCCTTCTTCACTT; reverse: GGGTCAATAGAAGGACACATCAC), collagen type I alpha 1 chain (*COL1A1*; forward: AGGGACACAGAGGTTTCAGT; reverse: AGCACCATCATTTCCACGAG), secreted phosphoprotein 1 (*SPP1*; forward: AGACACATATGATGGCCGAGG; reverse: GGCCTTGTATGCACCATTCAA), podoplanin (*PDPN*; forward: TTACTAGCCATCGGCTTCATTG; reverse: GGCGAGTACCTTCCCGACAT), RUNX family transcription factor 2 (*RUNX2*; forward: CCTCCTACCTGAGCCAGATG; reverse: ATGAAATGCTTGGGAACTGC), dickkopf WNT signaling pathway inhibitor 1 (*DKK1*; forward: TAGAGTCTAGAACGCAAGGATCTC; reverse: CAAAAACTATCACAGCCTAAAGGG), integrin binding sialoprotein (*IBSP*; forward: TGCCTTGAGCCTGCTTC; reverse: GCAAAATTAAAGCAGTCTTCATTTTG), bone gamma-carboxyglutamate protein (*BGLAP*; forward: GATGTGGTCAGCCAACTC; reverse: ACACTCCTCGCCCTATTG), alkaline phosphatase, biomineralization associated (*ALPL*; forward: ACCATTCCCACGTCTTCACATTTG; reverse: AGACATTCTCTCGTTCACCGCC), dentin matrix acidic phosphoprotein 1 (*DMP1*; forward: ACCAAGATGACAATGACTGCC; reverse: CAAGTGTAATGTCCAGCAATTCCT), sclerostin (*SOST*; forward: AGAGTACCCCGAGCCTCC; reverse: AGCTGTACTCGGACACGTCTTTG), kallikrein related peptidase 3 (*KLK3*; forward: AGTGCGAGAAGCATTCCCAAC; reverse: CCAGCAAGATCACGCTTTTGTT), androgen receptor (*AR*; forward: CTGGACACGACAACAACCAG; reverse: CAGATCAGGGGCGAAGTAGA), dopa decarboxylase (*DDC*; forward: CAAGTCACTCCCGGCTGC; reverse: CTCCTTCCCTCTCCTTCGGA), snail family transcriptional repressor 2 (*SNAI2*; forward: GGGGAGAAGCCTTTTTCTTG; reverse: TCCTCATGTTTGTGCAGGAG), (*DPP4*; forward: CAAATTGAAGCAGCCAGACA; reverse: CACACTTGAACACGCCACTT), retinol-binding protein 4 (*RBP4*; forward: AGGAGAACTTCGACAAGGCTC; reverse: GAGAACTCCGCGACGATGTT), mitochondrial ribosomal protein L42 (*MRPL42*; forward: ATCGGGTGTCCGCACTAAGTT; reverse: CAGCACGGGAGTTTTGACCT), and ribosomal protein L32 (*RPL32*; forward: GCACCAGTCAGACCGATATG; reverse: ACTGGGCAGCATGGCTTTG).

Protein analysis

Secretome analysis was performed on the conditioned media (2.5 ml) of PCa/hOBMT cocultures after 10 days coculture with either

LNCaP or C4-2B under various drug treatments and compared with monocultures, cultured in the same conditions, using a cytokine protein array (Profiler Human XL Cytokine Array Kit, Thermo Fisher Scientific) according to the manufacturer's instructions, and after protein concentrations were measured by the bicinchoninic acid assay (Thermo Fisher Scientific). Conditioned media were diluted to equivalent amount among samples and 1.5 was used for analysis. Membranes were exposed to x-ray for 5 min (ChemiDoc XRS+ with ImageLab 5.1 Software, Bio-Rad) and quantitatively analyzed using ImageJ. Results were expressed as the means of relative intensity (%) of duplicate spots relative to the mean intensity of three positive control spots of each array. Analysis was performed with two technical replicates and with hOBMT constructs made from cells from two different donors.

Statistical analysis

All statistical analyses were performed in IBM SPPS Statistics 23 (IBM Corp.) using a univariate general linear model and assessing parameter estimates when overall significance was achieved. Significance level was determined as $*P < 0.05$, $**P < 0.01$, $***P < 0.001$, and $****P < 0.0001$.

SUPPLEMENTARY MATERIALS

Supplementary material for this article is available at http://advances.sciencemag.org/cgi/content/full/7/27/eabg2564/DC1

View/request a protocol for this paper from *Bio-protocol*.

REFERENCES AND NOTES

1. B. A. Gartrell, F. Saad, Managing bone metastases and reducing skeletal related events in prostate cancer. *Nat. Rev. Clin. Oncol.* **11**, 335–345 (2014).
2. J. J. Body, S. Casimiro, L. Costa, Targeting bone metastases in prostate cancer: Improving clinical outcome. *Nat. Rev. Urol.* **12**, 340–356 (2015).
3. C. A. Heinlein, C. Chang, Androgen receptor in prostate cancer. *Endocr. Rev.* **25**, 276–308 (2004).
4. L. Wu, S. Xiang, X. Hu, M. Mo, C. Zhao, Y. Cai, S. Tong, H. Jiang, L. Chen, Z. Wang, W. Xiong, Z. Ou, Prostate-specific antigen modulates the osteogenic differentiation of MSCs via the cadherin 11-Akt axis. *Clin. Transl. Med.* **10**, 363–373 (2020).
5. Y. Ito, M. D. Sadar, Enzalutamide and blocking androgen receptor in advanced prostate cancer: Lessons learnt from the history of drug development of antiandrogens. *Res. Rep. Urol.* **10**, 23–32 (2018).
6. C. J. Logothetis, S. H. Lin, Osteoblasts in prostate cancer metastasis to bone. *Nat. Rev. Cancer* **5**, 21–28 (2005).
7. M. A. Augello, R. B. Den, K. E. Knudsen, AR function in promoting metastatic prostate cancer. *Cancer Metastasis Rev.* **33**, 399–411 (2014).
8. J. J. Yin, Y. N. Liu, H. Tillman, B. Barrett, S. Hewitt, K. Ylaya, L. Fang, R. Lake, E. Corey, C. Morrissey, R. Vessella, K. Kelly, AR-regulated TWEAK-FN14 pathway promotes prostate cancer bone metastasis. *Cancer Res.* **74**, 4306–4317 (2014).
9. X. Zhang, Interactions between cancer cells and bone microenvironment promote bone metastasis in prostate cancer. *Cancer Commun.* **39**, 76 (2019).
10. A. Vander Ark, J. Cao, X. Li, Mechanisms and approaches for overcoming enzalutamide resistance in prostate cancer. *Front. Oncol.* **8**, 180 (2018).
11. S. C. Lin, L. Y. Yu-Lee, S. H. Lin, Osteoblastic factors in prostate cancer bone metastasis. *Curr. Osteoporos. Rep.* **16**, 642–647 (2018).
12. M. Wang, F. Xia, Y. Wei, X. Wei, Molecular mechanisms and clinical management of cancer bone metastasis. *Bone Res.* **8**, 30 (2020).
13. H. Qiao, T. Tang, Engineering 3D approaches to model the dynamic microenvironments of cancer bone metastasis. *Bone Res.* **6**, 3 (2018).
14. F. Salamanna, D. Contartese, M. Maglio, M. Fini, A systematic review on in vitro 3d bone metastases models. A new horizon to recapitulate the native clinical scenario? *Oncotarget* **7**, 44803–44820 (2016).
15. M. H. Zaman, The role of engineering approaches in analysing cancer invasion and metastasis. *Nat. Rev. Cancer* **13**, 596–603 (2013).
16. N. Bock, A. Shokoohmand, T. Kryza, J. Röhl, J. Meijer, P. A. Tran, C. C. Nelson, J. A. Clements, D. W. Hutmacher, Engineering osteoblastic metastases to delineate the adaptive response of androgen-deprived prostate cancer in the bone metastatic microenvironment. *Bone Res.* **7**, 13 (2019).
17. A. Shokoohmand, J. Ren, J. Baldwin, A. Atack, A. Shafiee, C. Theodoropoulos, M.-L. Wille, P. A. Tran, L. J. Bray, D. Smith, N. Chetty, P. M. Pollock, D. W. Hutmacher, J. A. Clements, E. D. Williams, N. Bock, Microenvironment engineering of osteoblastic bone metastases reveals osteomimicry of patient-derived prostate cancer xenografts. *Biomaterials* **220**, 119402 (2019).
18. J. Shankar, A. Messenberg, J. Chan, T. M. Underhill, L. J. Foster, I. R. Nabi, Pseudopodial actin dynamics control epithelial-mesenchymal transition in metastatic cancer cells. *Cancer Res.* **70**, 3780–3790 (2010).
19. G. Moreno-Bueno, H. Peinado, P. Molina, D. Olmeda, E. Cubillo, V. Santos, J. Palacios, F. Portillo, A. Cano, The morphological and molecular features of the epithelial-to-mesenchymal transition. *Nat. Protoc.* **4**, 1591–1613 (2009).
20. N. Bock, J. Rohl, in *Methods in Molecular Biology* (2019).
21. Y. Lee, E. Schwarz, M. Davies, M. Jo, J. Gates, J. Wu, X. Zhang, J. R. Lieberman, Differences in the cytokine profiles associated with prostate cancer cell induced osteoblastic and osteolytic lesions in bone. *J. Orthop. Res.* **21**, 62–72 (2003).
22. C. D. Paul, P. Mistriotis, K. Konstantopoulos, Cancer cell motility: Lessons from migration in confined spaces. *Nat. Rev. Cancer* **17**, 131–140 (2017).
23. K. Jung, M. Lein, C. Stephan, K. Von Hosslin, A. Semjonow, P. Sinha, S. A. Loening, D. Schnorr, Comparison of 10 serum bone turnover markers in prostate carcinoma patients with bone metastatic spread: Diagnostic and prognostic implications. *Int. J. Cancer* **111**, 783–791 (2004).
24. B. Garcia-Fontana, S. Morales-Santana, M. Varsavsky, A. Garcia-Martin, J. A. Garcia-Salcedo, R. Reyes-Garcia, M. Munoz-Torres, Sclerostin serum levels in prostate cancer patients and their relationship with sex steroids. *Osteoporos. Int.* **25**, 645–651 (2014).
25. K. Margiotti, L. A. Wafa, H. Cheng, G. Novelli, C. C. Nelson, P. S. Rennie, Androgen-regulated genes differentially modulated by the androgen receptor coactivator L-dopa decarboxylase in human prostate cancer cells. *Mol. Cancer* **6**, 38 (2007).
26. X. Xu, L. A. Gurski, C. Zhang, D. A. Harrington, M. C. Farach-Carson, X. Jia, Recreating the tumor microenvironment in a bilayer, hyaluronic acid hydrogel construct for the growth of prostate cancer spheroids. *Biomaterials* **33**, 9049–9060 (2012).
27. E. L. Fong, X. Wan, J. Yang, M. Morgado, A. G. Mikos, D. A. Harrington, N. M. Navone, M. C. Farach-Carson, A 3D in vitro model of patient-derived prostate cancer xenograft for controlled interrogation of in vivo tumor-stromal interactions. *Biomaterials* **77**, 164–172 (2016).
28. P. S. Thakuri, C. Liu, G. D. Luker, H. Tavana, Biomaterials-based approaches to tumor spheroid and organoid modeling. *Adv. Healthc. Mater.* **7**, e1700980 (2018).
29. T. Bellido, J. Delgado-Calle, Ex vivo organ cultures as models to study bone biology. *JBMR Plus* **4**, 1–10 (2020).
30. N. Bock, in *Methods in Molecular Biology* (Humana Press Inc., 2019), vol. 2054, pp. 23–57.
31. N. Bock, J. Röhl, Real-time and 3D quantification of cancer cell dynamics: Exploiting a bioengineered human bone metastatic microtissue. *Methods Mol. Biol.* **2054**, 59–77 (2019).
32. E. Efstathiou, M. Titus, S. Wen, P. Troncoso, A. Hoang, P. Corn, I. Prokhorova, J. Araujo, C. Dmuchowski, A. Melhem-Bertrandt, S. Patil, C. J. Logothetis, Enzalutamide in combination with abiraterone acetate in bone metastatic castration-resistant prostate cancer patients. *Eur. Urol. Oncol.* **3**, 119–127 (2020).
33. C. Tran, S. Ouk, N. J. Clegg, Y. Chen, P. A. Watson, V. Arora, J. Wongvipat, P. M. Smith-Jones, D. Yoo, A. Kwon, T. Wasielewska, D. Welsbie, C. D. Chen, C. S. Higano, T. M. Beer, D. T. Hung, H. I. Scher, M. E. Jung, C. L. Sawyers, Development of a second-generation antiandrogen for treatment of advanced prostate cancer. *Science* **324**, 787–790 (2009).
34. T. M. Beer, A. J. Armstrong, D. E. Rathkopf, Y. Loriot, C. N. Sternberg, C. S. Higano, P. Iversen, S. Bhattacharya, J. Carles, S. Chowdhury, I. D. Davis, J. S. de Bono, C. P. Evans, K. Fizazi, A. M. Joshua, C.-S. Kim, G. Kimura, P. Mainwaring, H. Mansbach, K. Miller, S. B. Noonberg, F. Perabo, D. Phung, F. Saad, H. I. Scher, M.-E. Taplin, P. M. Venner, B. Tombal, Enzalutamide in metastatic prostate cancer before chemotherapy. *N. Engl. J. Med.* **371**, 424–433 (2014).
35. D. Vanderschueren, L. Vandenput, S. Boonen, M. K. Lindberg, R. Bouillon, C. Ohlsson, Androgens and bone. *Endocr. Rev.* **25**, 389–425 (2004).
36. M. Bienz, F. Saad, Androgen-deprivation therapy and bone loss in prostate cancer patients: A clinical review. *BoneKEy Rep.* **4**, 716 (2015).
37. A. J. Armstrong, M. Al-Adhami, P. Lin, T. Parli, J. Sugg, J. Steinberg, B. Tombal, C. N. Sternberg, J. De Bono, H. I. Scher, T. M. Beer, in *JAMA Oncology* (American Medical Association, 2020), vol. 6, pp. 217–225.
38. E. Sariisik, D. Zistl, D. Docheva, A. F. Schilling, M. Benoit, S. Sudhop, H. Clausen-Schaumann, Inadequate tissue mineralization promotes cancer cell attachment. *PLOS ONE* **15**, e0237116 (2020).
39. J. Hoffman-Censits, W. K. Kelly, Enzalutamide: A novel antiandrogen for patients with castrate-resistant prostate cancer. *Clin. Cancer Res.* **19**, 1335–1339 (2013).
40. A. Ghanem, Y. Lu, T. Cai, X. Mu, "Overexpression of RBP4 promotes proliferation, differentiation and mineralization of MC3T3-E1" (2017); www.ijcep.com/.

41. W. C. Huang, Z. Xie, H. Konaka, J. Sodek, H. E. Zhau, L. W. K. Chung, Human osteocalcin and bone sialoprotein mediating osteomimicry of prostate cancer cells: Role of cAMP-dependent protein kinase A signaling pathway. *Cancer Res.* **65**, 2303–2313 (2005).
42. K. S. Koeneman, F. Yeung, L. W. K. Chung, Osteomimetic properties of prostate cancer cells: A hypothesis supporting the predilection of prostate cancer metastasis and growth in the bone environment. *Prostate* **39**, 246–261 (1999).
43. N. Blaszczyk, B. A. Masri, N. R. Mawji, T. Ueda, G. McAlinden, C. P. Duncan, N. Bruchovsky, H. U. Schweikert, D. Schnabel, E. C. Jones, M. D. Sadar, Osteoblast-derived factors induce androgen-independent proliferation and expression of prostate-specific antigen in human prostate cancer cells. *Clin. Cancer Res.* **10**, 1860–1869 (2004).
44. A. Sebastian, N. R. Hum, B. D. Hudson, G. G. Loots, Cancer-osteoblast interaction reduces sost expression in osteoblasts and up-regulates lncRNA MALAT1 in prostate cancer. *Microarrays* **4**, 503–519 (2015).
45. T. A. Guise, K. S. Mohammad, G. Clines, E. G. Stebbins, D. H. Wong, L. S. Higgins, R. Vessella, E. Corey, S. Padalecki, L. Suva, J. M. Chirgwin, Basic mechanisms responsible for osteolytic and osteoblastic bone metastases. *Clin. Cancer Res.* **12**, 6213s–6216s (2006).
46. E. Godebu, M. Muldong, A. Strasner, C. N. Wu, S. C. Park, J. R. Woo, W. Ma, M. A. Liss, T. Hirata, O. Raheem, N. A. Cacalano, A. A. Kulidjian, C. A. M. Jamieson, PCSD1, a new patient-derived model of bone metastatic prostate cancer, is castrate-resistant in the bone-niche. *J. Transl. Med.* **12**, 275 (2014).
47. D. Burner, T. Mendoza, M. Muldong, S. Lee, C. Arreola, O. Miakicheva-Greenburg, W. Zhu, C. Wu, N. Cacalano, C. Jamieson, C. Kane, A. Kulidjian, C. Jamieson, MP81-19 mechanisms of anti-androgen resistance in a 3D patient-derived organoid model of bone metastatic prostate cancer. *J. Urol.* **201**, e1179–e1180 (2019).
48. C. Sun, Y. Shi, L. L. Xu, C. Nageswararao, L. D. Davis, T. Segawa, A. Dobi, D. G. McLeod, S. Srivastava, Androgen receptor mutation (T877A) promotes prostate cancer cell growth and cell survival. *Oncogene* **25**, 3905–3913 (2006).
49. P. Msaouel, G. Nandikolla, S. G. Pneumaticos, M. Koutsilieris, Bone microenvironment-targeted manipulations for the treatment of osteoblastic metastasis in castration-resistant prostate cancer. *Expert Opin. Investig. Drugs* **22**, 1385–1400 (2013).
50. Y. X. Sun, A. Schneider, Y. Jung, J. Wang, J. Dai, J. Wang, K. Cook, N. I. Osman, A. J. Koh-Paige, H. Shim, K. J. Pienta, E. T. Keller, L. K. McCauley, R. S. Taichman, Skeletal localization and neutralization of the SDF-1(CXCL12)/CXCR4 axis blocks prostate cancer metastasis and growth in osseous sites in vivo. *J. Bone Miner. Res.* **20**, 318–329 (2005).
51. M. J. Wilson, R. Haller, S. Y. Li, J. W. Slaton, A. A. Sinha, N. F. Wasserman, Elevation of dipeptidylpeptidase IV activities in the prostate peripheral zone and prostatic secretions of men with prostate cancer: Possible prostate cancer disease marker. *J. Urol.* **174**, 1124–1128 (2005).
52. C. Shah, Y. R. Hong, R. Bishnoi, A. Ali, W. P. Skelton, L. H. Dang, J. Huo, N. H. Dang, Impact of DPP4 inhibitors in survival of patients with prostate, pancreas, and breast cancer. *Front. Oncol.* **10**, 405 (2020).
53. Y. Wang, Y. Wang, Z. Zhang, Adipokine RBP4 drives ovarian cancer cell migration. *J. Ovarian Res.* **11**, 29 (2018).
54. H. Uehara, T. Takahashi, K. Izumi, Induction of retinol-binding protein 4 and placenta-specific 8 expression in human prostate cancer cells remaining in bone following osteolytic tumor growth inhibition by osteoprotegerin. *Int. J. Oncol.* **43**, 365–374 (2013).

Acknowledgments: We acknowledge the Translational Research Institute for the excellent core facilities that enabled this research, in particular, A. Ju, TRI microscopy facility. We also thank J. Malayil and T. Yarlagadda for scaffold production, treatment, and coating; C. Theodoropoulos, F. Lawrence, the CARF histology facility from IHBI (QUT), and S.-A. Stephenson (QUT) for the mKO2 vector; and R. Crawford (QUT) for providing human bone samples. **Funding:** N.B. was supported by IHBI ECR grant, Advance Queensland (AQ) Maternity Fund Award from the Queensland Government (DSITI), Young Researcher Award (2017-YR-RoW-9) from Lush (UK), supporting nonanimal testing alternatives, National Health and Medical Research Council (NHMRC) Peter Doherty Early Career Research Fellowship (RF) (APP1091734), and John Mills Young Investigator Award (YI0715) from the Prostate Cancer Foundation of Australia (PCFA) and JJ Richards & Sons via an In Vitro Excellence Research grant; J.A.C.: NHMRC PRF; D.W.H.: Humboldt RF, ARC Industrial Transformation Training Center in Additive Biomanufacturing (IC160100026), NHMRC, World Cancer Foundation, National Breast Cancer Foundation, and PCFA. D.W.H., J.A.C., and C.C.N.: Movember Revolutionary Team Award (from Movember and PCFA). APCRC-Q and the Translational Research Institute are supported by grants from the Australian Government. **Author contributions:** All authors confirmed that they have contributed to the intellectual content of this paper and have made significant contributions to some of the following: conception and design, acquisition of data, analysis and interpretation of data, and drafting or revising the article. In particular, N.B., T.K., A.S., D.W.H., and J.A.C contributed to study design. N.B. performed most of the experiments, analyzed and interpreted the data, and wrote the manuscript. T.K. and A.S. helped with experiment planning, data acquisition, and interpretation. J.R. and A.R. helped developing new protocols for data analysis and did several types of characterization. M.-L.W. developed a protocol for micro–computed analysis (μCT) and performed the μCT experiments and analysis. **Competing interests:** The authors declare that they have no competing interests. **Data and materials availability:** All data needed to evaluate the conclusions in the paper are present in the paper and/or the Supplementary Materials. Additional data related to this paper may be requested from the authors.

Submitted 22 December 2020
Accepted 17 May 2021
Published 30 June 2021
10.1126/sciadv.abg2564

Citation: N. Bock, T. Kryza, A. Shokoohmand, J. Röhl, A. Ravichandran, M.-L. Wille, C. C. Nelson, D. W. Hutmacher, J. A. Clements, In vitro engineering of a bone metastases model allows for study of the effects of antiandrogen therapies in advanced prostate cancer. *Sci. Adv.* **7**, eabg2564 (2021).